

Journal of Turbulence

Publication details, including instructions for authors and
subscription information:

<http://www.tandfonline.com/loi/tjot20>

Evolution of an asymmetric turbulent shear layer in a thermocline

Hieu T. Pham^a & Sutanu Sarkar^a

^a Department of Mechanical and Aerospace Engineering, UC San
Diego, La Jolla, CA, USA

Published online: 14 May 2014.

To cite this article: Hieu T. Pham & Sutanu Sarkar (2014) Evolution of an asymmetric
turbulent shear layer in a thermocline, *Journal of Turbulence*, 15:7, 449-471, DOI:
[10.1080/14685248.2014.914216](https://doi.org/10.1080/14685248.2014.914216)

To link to this article: <http://dx.doi.org/10.1080/14685248.2014.914216>

PLEASE SCROLL DOWN FOR ARTICLE

Taylor & Francis makes every effort to ensure the accuracy of all the information (the
“Content”) contained in the publications on our platform. However, Taylor & Francis,
our agents, and our licensors make no representations or warranties whatsoever as to
the accuracy, completeness, or suitability for any purpose of the Content. Any opinions
and views expressed in this publication are the opinions and views of the authors,
and are not the views of or endorsed by Taylor & Francis. The accuracy of the Content
should not be relied upon and should be independently verified with primary sources
of information. Taylor and Francis shall not be liable for any losses, actions, claims,
proceedings, demands, costs, expenses, damages, and other liabilities whatsoever
or howsoever caused arising directly or indirectly in connection with, in relation to or
arising out of the use of the Content.

This article may be used for research, teaching, and private study purposes. Any
substantial or systematic reproduction, redistribution, reselling, loan, sub-licensing,
systematic supply, or distribution in any form to anyone is expressly forbidden. Terms &
Conditions of access and use can be found at [http://www.tandfonline.com/page/terms-
and-conditions](http://www.tandfonline.com/page/terms-and-conditions)

Evolution of an asymmetric turbulent shear layer in a thermocline

Hieu T. Pham* and Sutanu Sarkar

Department of Mechanical and Aerospace Engineering, UC San Diego, La Jolla, CA, USA

(Received 6 January 2014; accepted 6 April 2014)

Large eddy simulations are used to examine the evolution of a shear layer in a thermocline with non-uniform density stratification. Unlike previous studies, the density in the present study is continuously stratified and has stratification in the upper half different from the lower half of the shear layer. The stratification in the upper half is fixed at $J_u = 0.05$, while the stratification in the lower half is increased to $J_d = 0.05, 0.15, 0.25$ and 0.35 , leading to a progressively stronger asymmetry of the Ri_g profile in the four cases. Here, J is the bulk Richardson number and Ri_g is the gradient Richardson number. The type of shear instability and the properties of the ensuing turbulence are found to depend strongly on the degree of asymmetry in stratification. The shear instability changes from a Kelvin–Helmholtz (KH) mode at $J_d = 0.05$ to a Holmboe (H) mode at $J_d = 0.35$ and exhibits characteristics of both KH and H modes at intermediate values of J_d . Differences in the evolution among the cases are quantified using density visualisations and statistics such as mean shear, mean stratification and turbulent kinetic energy.

Keywords: stratified shear layer; turbulence

1. Introduction

Shear instability in a stratified environment plays an important role in many geophysical flows by providing a pathway to turbulence and mixing. In river plumes, shear instability observed at the interface between fresh river water and salty ocean water influences how the plumes spread into an open ocean [1]. Transition layers that separate the surface mixed layer from the deeper ocean mediate the vertical exchanges of mass, momentum and energy between the deep ocean and the atmosphere [2]. In the Equatorial Undercurrents (EUC) where turbulent mixing can alter the cycle of El Niño Southern Oscillations, shear instability is believed to be the main mechanism that drives the observed intense mixing [3,4]. Therefore, it is important to study the evolution of shear instabilities and turbulence in these environmental applications.

Shear instability and ensuing turbulence in stratified fluids has been studied intensively using linear stability analysis (LSA), numerical simulations and laboratory experiments [5–13]. However, the majority of the studies focus on the parallel shear flow between two streams having different but constant density. The centres of the profiles of shear and density gradient coincide and the profiles are symmetric with respect to their common centre. When the thicknesses of velocity and density interfaces are comparable, the evolution of the shear layer exhibits the formation of Kelvin–Helmholtz (KH) billows and their subsequent breakdown into turbulence [9]. When the thickness of the density interface is significantly smaller than that of the velocity interface, a symmetric Holmboe (H) instability develops.

*Corresponding author. Email: h8pham@ucsd.edu

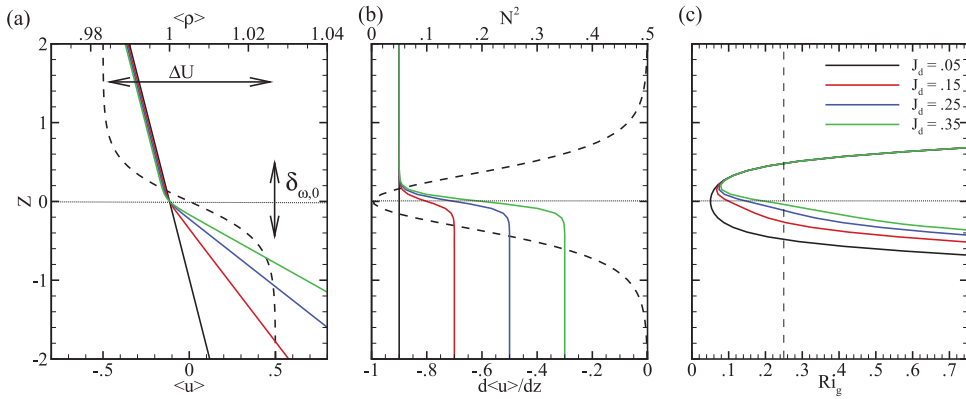


Figure 1. *Initial* mean profiles exhibit a canonical hyperbolic tangent shear layer in which stratification in the lower half varies among four cases: (a) streamwise velocity (u) (dashed) and density (ρ) (solid); (b) shear $d\langle u \rangle/dz$ (dashed) and squared buoyancy frequency N^2 (solid); and (c) gradient Richardson number Ri_g . Colours denote the four cases with different stratification in the bottom half of the shear layer, $J_d = 0.05$ (black), 0.15 (red), 0.25 (blue) and 0.35 (green).

In the context of LSA of this flow, a KH mode has zero phase speed, while the H mode has a finite phase speed. The nonlinear evolution of the H mode exhibits density wisps and cusps [12] rather than the overturning of the central isopycnal seen in the case of the KH mode. In geophysical flows, the density often varies asymmetrically throughout and beyond the shear layer in a complex manner. It is therefore necessary to go beyond these canonical examples to flows where the background density gradient is asymmetric with respect to the centre of the sheared region, e.g. the configuration of Figure 1 which corresponds to an upper ocean shear layer in a pycnocline.

Carpenter et al. [14] use direct numerical simulations (DNSs) to investigate the evolution of shear instability in flows where, different from Figure 1, the asymmetry is due to a symmetric sheared region being vertically displaced from a symmetric region of density gradient. We will refer to the configuration of Carpenter et al. [14] as a case with an eccentric stratification profile. Unlike the sharp transition between KH and H instabilities seen in the case with coincident centres of shear and density interfaces, a gradual transition from KH-type overturning to gentler H-type density wisps is found as the distance between the interfaces increases. LSA of this case with eccentric stratification does not show a clear change from zero to non-zero instability phase speed and nonlinear evolution shows shear instability with both KH and H characteristics during the gradual transition from the KH to H mode. Carpenter et al. [15] explain the transition from the KH to H mode by splitting the growth rate into a KH contribution and an H contribution based on interpreting the instability as the result of the interaction of independently propagating interfacial waves. At low stratification, the KH contribution is the largest. At large stratification, the H contribution is the largest. At intermediate stratification, both KH and H modes contribute to the growth rate in the asymmetric case, leading to mixed characteristics and a gradual transition from the KH to H mode with increasing stratification. In contrast, the analysis of the case with concentric shear and density profiles shows that the KH growth rate decreases sharply at the same point that the H growth rate increases sharply, resulting in a sharp transition between KH and H instability modes.

The density profiles used in the aforementioned studies of transition from KH to H instability have zero gradient in regions outside the shear layer and, therefore, vertically

propagating internal waves found in situations with stratification outside the sheared region [16–19] are absent. Pham et al. [19] use DNSs to reveal energetic wave fields in regions below the shear layer where the stratification is sufficiently larger than inside the shear layer, and to show that the nonlinear evolution of the shear instability is significantly modified owing to the presence of wave radiation. Even though the stratification profile in Pham et al. [19] is asymmetric with respect to the shear layer centre, the density gradient is uniform throughout the shear layer and only KH shear instability is observed. In an attempt to simulate shear instability in the EUC, Pham et al. [4] present a single DNS in which the density gradient varies asymmetrically inside the shear layer. The study shows the development of asymmetric H instability in the upper weakly stratified portion of the shear layer, while internal waves are noted in the lower strongly stratified portion. The present work goes beyond [4] by exploring how different levels of stratification inside the shear layer can affect the evolution of asymmetric shear instability.

A parallel shear flow with an asymmetric density gradient inside the shear layer is considered, as shown in Figure 1. Cases with different levels of stratification are simulated and, as can be seen, KH and H modes as well as transitional modes are present depending on the level of stratification. The evolution of coherent structures such as billows and density wisps as well as the excitation of internal waves is contrasted among the cases. Profiles of shear, density gradient, gradient Richardson number as well as the budgets of turbulent kinetic energy (TKE) are examined in each case so that turbulence can be quantified for each type of shear instability.

2. Model setup

In the present study, we consider a parallel shear flow between two streams flowing in opposing directions, as shown in Figure 1(a). The streamwise velocity $\langle u^* \rangle$ has a hyperbolic tangent profile with a velocity difference ΔU^* and an initial thickness $\delta_{\omega,0}^*$ as follows:

$$\langle u^* \rangle(z^*) = \frac{\Delta U^*}{2} \tanh\left(\frac{z^*}{0.5\delta_{\omega,0}^*}\right).$$

The thickness of the shear layer δ_{ω}^* is defined as $\Delta U^*/\max(|d\langle u^* \rangle/dz^*|)$. Here, we use the superscript $*$ to denote dimensional quantities, subscript 0 to denote initial quantities at time $t^* = 0$ and angle brackets $\langle \cdot \rangle$ to indicate quantities that are horizontally averaged in the streamwise (x) and spanwise (y) directions.

The density profiles ρ^* have a sharp interface at the centre of the shear layer which separates a weakly stratified upper half from a strongly stratified lower half. The profiles of squared buoyancy frequency $N^{*2} = -g^*/\rho_0^* d\langle \rho^* \rangle/dz^*$ shown in Figure 1(b) are described by the following expression:

$$N^{*2}(z) = \frac{N_u^{*2} + N_d^{*2}}{2} + \frac{N_u^{*2} - N_d^{*2}}{2} \tanh\left(\frac{z^*}{0.1\delta_{\omega,0}^*}\right),$$

where N_u^{*2} and N_d^{*2} are the squared buoyancy frequencies in the upper and lower halves of the shear layer, respectively.

Using the velocity difference ΔU^* , the thickness $\delta_{\omega,0}^*$ and $\rho_0^* \delta_{\omega,0}^* N_u^{*2} / g$ as the characteristic velocity, length and density scales, respectively, the large eddy simulation (LES) equations for filtered motion take the following non-dimensional forms:

Mass:

$$\frac{\partial \bar{u}_j}{\partial x_j} = 0, \quad (1)$$

Momentum:

$$\frac{\partial \bar{u}_i}{\partial t} + \frac{\partial (\bar{u}_j \bar{u}_i)}{\partial x_j} = -\frac{\partial \bar{P}}{\partial x_i} + \frac{1}{Re_0} \frac{\partial^2 \bar{u}_i}{\partial x_j \partial x_j} - J_u \bar{\rho}' - \frac{\partial \tau_{ij}}{\partial x_j}, \quad (2)$$

Density:

$$\frac{\partial \bar{\rho}}{\partial t} + \frac{\partial (\bar{u}_j \bar{\rho})}{\partial x_j} = \frac{1}{Re_0 Pr} \frac{\partial^2 \bar{\rho}}{\partial x_j \partial x_j} - \frac{\partial Q_j}{\partial x_j}, \quad (3)$$

where the overbar denotes filtered quantities and g denotes the gravity acting in the vertical (z) direction. The subgrid stress τ_{ij} and subgrid buoyancy flux Q_j are to be parameterised by an LES model. The non-dimensional parameters in this flow are: Reynolds number $Re_0 = \Delta U^* \delta_{\omega,0}^* / \nu^*$, Richardson number in the upper half of the shear layer $J_u = N_u^{*2} \delta_{w,o}^{*2} / \Delta U^{*2}$ and Prandtl number $Pr = \nu^* / \kappa^*$, where ν^* and κ^* are the molecular viscosity and diffusivity, respectively.

Four simulations are performed at $Re_0 = 5000$, $Pr = 7$ and $J_u = 0.05$. While fixing J_u in all cases, the stratification J_d in the lower half of the shear layer is varied between the cases to create asymmetry in the variation of gradient Richardson number, $Ri_g = N^2 / S^2$, within the shear layer, as shown in [Figure 1](#). In the case of $J_d = 0.05$, the shear layer has uniform stratification, and this case with a symmetric profile of Ri_g is taken as the base case to be contrasted with the other asymmetric cases. The resulting gradient Richardson number profiles shown in [Figure 1\(c\)](#) have their minimum value displaced further into the upper half of the shear layer as J_d increases. The objective of the present study is to investigate how the asymmetry of the initial Ri_g profiles affects the evolution of shear instability and turbulence in the shear layer.

The present study adopts the dynamic eddy viscosity model as described in Germano et al. [20] to compute the subgrid stresses and subgrid buoyancy fluxes. The subgrid stresses and subgrid buoyancy fluxes are implemented as follows:

$$\tau_{ij} = -2C_d \bar{\Delta}^2 |\bar{S}| \bar{S}_{ij} \quad (4)$$

and

$$Q_j = -C_\theta \bar{\Delta}^2 |\bar{S}| \frac{\partial \bar{\rho}}{\partial x_j}, \quad (5)$$

where $\bar{\Delta}$ is the filter width, $\bar{S}_{ij} = 1/2 (\partial \bar{u}_i / \partial x_j + \partial \bar{u}_j / \partial x_i)$ is the resolved strain rate tensor and $|\bar{S}|$ is defined as $\sqrt{2\bar{S}_{ij}\bar{S}_{ij}}$. The subgrid eddy viscosity and diffusivity are given by

$$\nu_{\text{sgs}} = C_d \bar{\Delta}^2 |\bar{S}|, \tag{6}$$

$$\kappa_{\text{sgs}} = C_\theta \bar{\Delta}^2 |\bar{S}|, \tag{7}$$

respectively. The model coefficients C_d and C_θ are determined by a dynamic procedure in which a test filter is applied to the resolved velocity and density fields. Quantities denoted by $\hat{\cdot}$ are double filtered with both the test and LES filters. The dynamic coefficients are given by

$$C_d = -\frac{1}{2} \frac{\langle L_{ij} M_{ij} \rangle}{\langle M_{ij} M_{ij} \rangle},$$

$$C_\theta = -\frac{1}{2} \frac{\langle L_i^\theta M_i^\theta \rangle}{\langle M_j^\theta M_j^\theta \rangle},$$

where

$$L_{ij} = \widehat{\bar{u}_i \bar{u}_j} - \widehat{\bar{u}_i} \widehat{\bar{u}_j},$$

$$M_{ij} = \widehat{\bar{\Delta}^2 |\bar{S}| \widehat{\bar{S}}_{ij}} - \bar{\Delta}^2 \widehat{|\bar{S}| \bar{S}_{ij}},$$

$$L_i^\theta = \widehat{\bar{\rho} \bar{u}_i} - \widehat{\bar{\rho}} \widehat{\bar{u}_i},$$

$$M_i^\theta = \widehat{\bar{\Delta}^2 |\bar{S}| \frac{\partial \bar{\rho}}{\partial x_i}} - \bar{\Delta}^2 \widehat{|\bar{S}| \frac{\partial \bar{\rho}}{\partial x_i}}.$$

The test filter is applied in physical space using an explicit three-point trapezoidal rule. The ratio of the test to LES filter width, $\hat{\Delta}/\bar{\Delta}$, is taken to be $\sqrt{6}$.

A computational domain of $L_x = 30.84$, $L_y = 7.8$ and $L_z = 107$ is discretised using a grid of $256 \times 64 \times 512$ points. The grid spacing is uniform in the x and y directions. The vertical grid spacing is uniform with $\Delta z = 0.06$ in the region $-5 < z < 5$ and stretched at a rate of 2% outside this region. The numerical methods used in the present study are similar to those in [21,22]. A second-order central difference in space and a third-order Runge–Kutta marching in time are used to integrate Equations (2)–(3). A multigrid Poisson solver is used to enforce an incompressibility condition. A sponge region is used in the regions $z < -40$ and $z > 40$ to prevent wave reflections from the upper and lower boundaries. During the early evolution of the KH billows and the H wisps, a sharp density gradient forms over just one grid point causing numerical oscillations on both sides of the gradient. An explicit top-hat filter is selectively applied to the density field at every 10 time steps to remove the oscillations. The filter is applied only at the nodes i where the following criteria are satisfied:

$$\kappa_{\text{sgs}}/\kappa < 0.5,$$

$$[\bar{\rho}(i+1) - \bar{\rho}(i)][\bar{\rho}(i) - \bar{\rho}(i-1)] < 0,$$

$$[\bar{\rho}(i+1) - \bar{\rho}(i)][\bar{\rho}(i) - \bar{\rho}(i-1)] < 0.$$

Here, i denotes the grid index, the double bars indicate the new filtered value of density, and the filtering is applied in all three directions. The use of selective criteria to improve the LES results at high Re has been discussed in Pham and Sarkar [23] who simulated the canonical shear layer between two free streams with different constant values of density. For convenience during discussion, we simplify the notation by dropping the asterisks and the overbars. Hereafter, parameters of interest are understood to be filtered and non-dimensional.

Small-amplitude broadband velocity perturbations are added to the mean velocity profile prescribed above to initiate the growth of shear instabilities. The perturbations have the following energy spectrum:

$$E(k) = \left(\frac{k}{k_0}\right)^4 \exp\left[-2\left(\frac{k}{k_0}\right)^2\right],$$

where k is the horizontal wavenumber and k_0 is set to be 20.0. The amplitude of the perturbations is $0.1\%\Delta U$. The horizontal boundaries have periodic conditions, while the top and bottom boundaries have the following conditions:

$$\begin{aligned} u(z_{\min}) &= \frac{1}{2}, & u(z_{\max}) &= -\frac{1}{2}, \\ v(z_{\min}) &= v(z_{\max}) = 0, \\ w(z_{\min}) &= w(z_{\max}) = 0, \\ \frac{\partial p}{\partial z}(z_{\min}) &= \frac{\partial p}{\partial z}(z_{\max}) = 0, \\ \frac{\partial \rho}{\partial z}(z_{\min}) &= -J_d, & \frac{\partial \rho}{\partial z}(z_{\max}) &= -J_u. \end{aligned}$$

In the following sections, we rely on the TKE budget to characterise the evolution of turbulence in the shear layer. Therefore, it is convenient to introduce in advance the TKE budget, which is described by the following equation:

$$\frac{dK}{dt} = P - \varepsilon + B - \frac{dT_3}{dz} - \frac{dT_{3,\text{sgs}}}{dz}, \quad (8)$$

where $K = 1/2 \langle u'_i u'_i \rangle$ is the TKE, P is the turbulent production,

$$P = -\langle u' w' \rangle \frac{d\langle u \rangle}{dz},$$

ε is the total dissipation rate consisting of resolved and subgrid contributions,

$$\varepsilon = \frac{2}{Re_0} \langle S'_{ij} S'_{ij} \rangle - \left\langle \tau'_{ij} \frac{\partial u'_i}{\partial x_j} \right\rangle,$$

and B is the buoyancy flux,

$$B = -J_u \langle \rho' w' \rangle.$$

The transport term dT_3/dz is defined with

$$T_3 = \frac{1}{2} \langle w' u'_i u'_i \rangle + \frac{\langle p' w' \rangle}{\rho_0} - \frac{2}{Re_0} \langle u'_i S'_{3i} \rangle$$

and the subgrid transport $dT_{3,sgs}/dz$ is defined with

$$T_{3,sgs} = \langle \tau'_{i3} u'_i \rangle.$$

3. Evolution of asymmetric shear instabilities

Simulations in the present study show the development of shear instabilities as the precursor to turbulence in all four cases. In this section, we provide visualisations of density fields to contrast the anatomy of different types of shear instability. Carpenter et al. [15] chose an eccentric configuration with relative displacement of the centre of a compact sheared region with respect to the centre of a compact density gradient region, while we choose a different configuration with the two regions above and below the centre of the shear layer having different values of density gradient. Nevertheless, both configurations have Ri_g profiles that are asymmetric with respect to the shear layer centre and, similar to [15], we find shear instabilities ranging from a pure KH mode through a transitional instability mode to a pure H mode.

In the symmetric case $J_d = 0.05$, KH shear instability is seen to develop as shown in Figure 2(a). An intrinsic property of a KH mode is the formation of billows in the centre of the shear layer. The billows lift heavy fluids up, push light fluids down and mix up the density interfaces inside the shear layer. Five billows are seen over the horizontal domain. The vertical extent of the billows becomes twice as large as the initial thickness δ_ω before the billows break down into smaller scale turbulence. KH billows can corotate and pair before the shear layer becomes turbulent. However, pairing does not occur in the present high- Re simulations. Billows at high Reynolds number are rapidly distorted by the growth of smaller scale fluctuations, as noted in Pham and Sarkar [24], that inhibit corotation and pairing.

In the asymmetric cases with higher stratification, $J_d = 0.15$ and 0.25 , the structure of the instability has a resemblance to KH billows, as shown in Figure 2(b) and 2(c). Similar to the symmetric case $J_d = 0.05$ in Figure 2(a), five billows are seen in the shear layer, indicating the wavelength of the most unstable mode has not changed as J_d increases. However, the vertical extent of the billows becomes smaller in the cases with stronger stratification. In the case of $J_d = 0.25$, the central isopycnal does not roll up and the billows only occupy the upper half of the shear layer, leaving the bottom half unmixed at this time. The growth rate of the shear instabilities also decreases with increasing stratification in the cases with KH billows. The density fields in Figure 2(b) are shown at times when the integrated production across the shear layer peaks. At these times, the billows reach their maximum size before transition to turbulence. The billows in the case of $J_d = 0.25$ reach their maximum size at the earliest time $t = 78$ which indicates the largest growth rate among the cases. In the cases of $J_d = 0.15$ and 0.25 , the billows have their maximum size at significantly later times owing to slower growth rates. It is worth noting that the growth rate discussed here is different from that obtained from LSA. The discussed growth rate includes both the growth of shear instability from infinitesimal perturbations as in LSA and the enlargement of the billows, which is a nonlinear process. The LSA of Carpenter

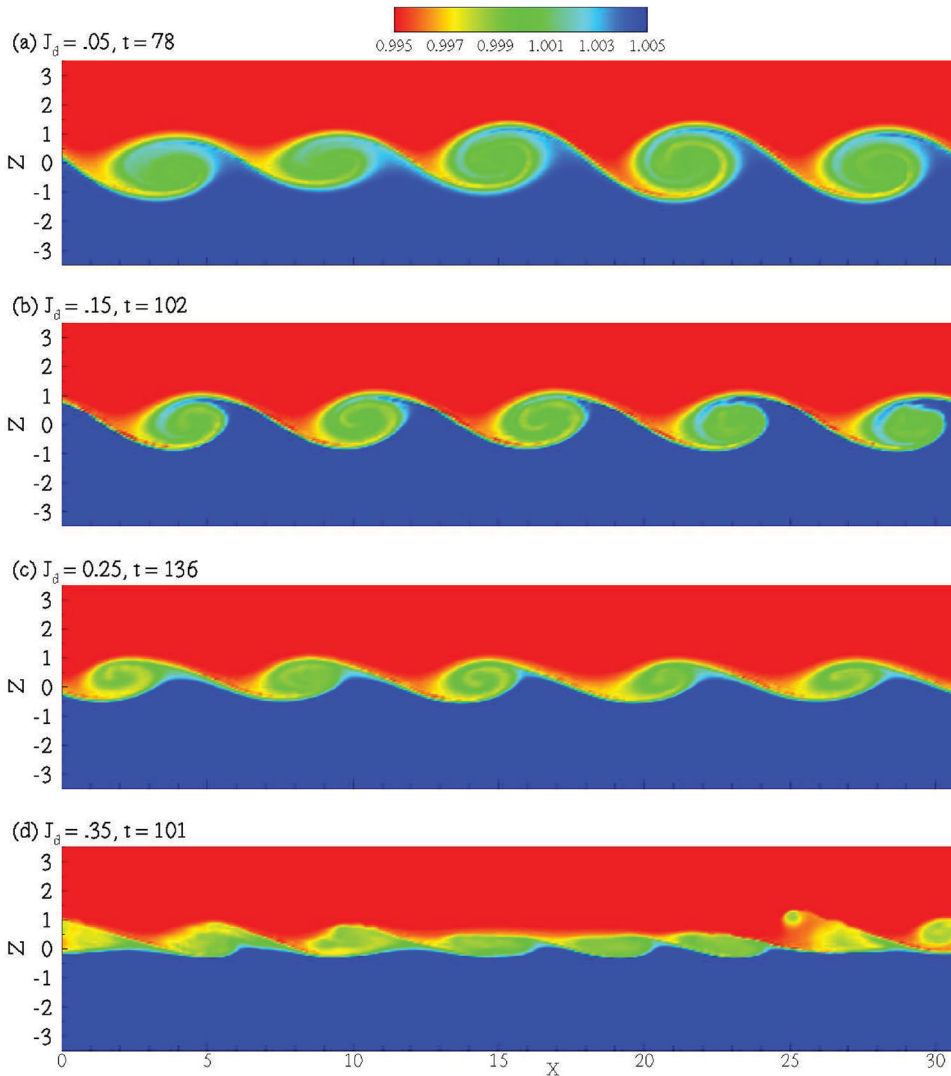


Figure 2. Snapshots of the density field contrast the evolution of shear instabilities in four cases. The snapshots are shown at times when the integrated production peaks. In the symmetric case of $J_d = 0.05$ (a), KH billows form in the shear layer with a roll-up and overturning of the central isopycnal. As J_d increases (b, c), the billows become smaller and concentrate toward the upper half of the shear layer. In the case of $J_d = 0.35$ (d), roll-up of the central isopycnal is replaced by H wisps that eject heavier fluid upward.

et al. [15] also supports the inhibition of growth rate when the stratification increases. That study further suggests that the contribution of H modes becomes larger with increasing stratification in the regime of transitional modes. The cases of $J_d = 0.15$ and 0.25 in the present study have the stratification belonging to the transition regime, and the development of the shear instabilities in these cases has characteristics similar to the results of Carpenter et al. [15], as discussed below.

In the case of $J_d = 0.35$, the instability exhibits features of an H shear instability, as shown in [Figure 2\(d\)](#). Unlike KH modes, the nonlinear evolution of an H mode includes formation of thin density wisps and cusps. While the KH billows vigorously stir and overturn the density interface inside the shear layer as in the case of $J_d = 0.05$, the wisps gently scour the interface. At times, the H shear instability ejects a volume of heavy fluid from the density interface upward into regions above the shear layer, as seen at $x = 25$ in [Figure 2\(d\)](#). Features of wisps and cusps and the upward ejection of heavy fluid have been discussed at length in previous studies [[4,11,12,14](#)]. The wavelength of the H instability in the case of $J_d = 0.25$ is shorter than the wavelength seen in the other cases. Seven wisps are seen to span the horizontal domain. Noting the time at which the peak integrated production occurs, $t = 101$, the growth rate of the H instability in the case of $J_d = 0.35$ is comparable to the rate in the case of $J_d = 0.15$, but significantly larger than the rate in the case of $J_d = 0.25$. By increasing the stratification from $J_d = 0.25$ to $J_d = 0.35$, the unstable shear layer moves from the transitional regime into the H regime. Features of KH modes observed in the other three cases are not seen in the case of $J_d = 0.35$.

Another key difference in the structure of the shear instabilities is in their phase speed. [Figure 3](#) shows the $x-t$ diagrams of a streamwise density probe taken at the centre of the shear layer, $z = 0$, in the four simulated cases. During the growth period of the instabilities, $t < 150$, coherent phase lines are observed in all cases. The tilt angle of the phase lines denotes the phase speeds of the shear instabilities. In the case of $J_d = 0.05$, the phase lines in [Figure 3\(a\)](#) are horizontal corresponding to a zero phase speed. The KH instability in this case is therefore stationary with respect to the simulation frame. In the other cases, the phase lines tilt leftward with a negative slope corresponding to a negative phase speed. The shear instabilities in these cases propagate toward the negative x direction. In the transitional regime, i.e. in the cases of $J_d = 0.15$ and 0.25 , increase in stratification also increases the (negative) phase speed. The phase speeds in the cases of $J_d = 0.25$ and 0.35 are similar. It is noted that the initial growth of the instabilities does not occur at the centre of the shear layer, $z = 0$, in all cases. The location of initial growth, namely instability levels, coincides with the depth where the phase speed of the instability matches with the mean streamwise velocity $\langle u \rangle$. In the case of $J_d = 0.05$, the phase speed is zero and $\langle u \rangle$ at $z = 0$ is also zero initially, so the instability level is at $z = 0$. In the other three cases, the phase speeds have negative values, so the instability levels progressively move upward into the upper half of the shear layer where $\langle u \rangle$ is negative. Recalling the initial Ri_g profiles in [Figure 1\(c\)](#), as J_d increases, the location of minimum Ri_g shifts upward similar to the instability level. In the present simulations, the instability level is found to coincide with the location of minimum Ri_g .

After the development of billows and wisps, the shear layer transitions into turbulence, as shown in [Figure 4\(a\)–\(d\)](#). The figures are taken at times when the dissipation integrated over the shear layer peaks. Turbulent fluctuations having a broad range of scales are seen in the shear layer. In the case of $J_d = 0.05$, after the breakdown of the primary KH billows, secondary density overturns are seen at the edges of the shear layer. For example, density overturns are seen at $x = 5$ and $x = 30$ at the lower edge of the shear layer in [Figure 4\(a\)](#). It is noted that the asymmetry in [Figure 4\(a\)](#) with overturns occurring only in the lower edge of the shear layer is due to intermittency. The overturns also occur at the upper edge of the shear layer at other times, and the resulting evolution of the mean shear layer is symmetric in this case. As J_d increases, turbulent fluctuations concentrate more in the upper half of the shear layer where the stratification is weaker, as can be seen in [Figure 4\(b\)–\(d\)](#). Secondary density overturns also occur intermittently at the lower edges of the shear layer in the cases

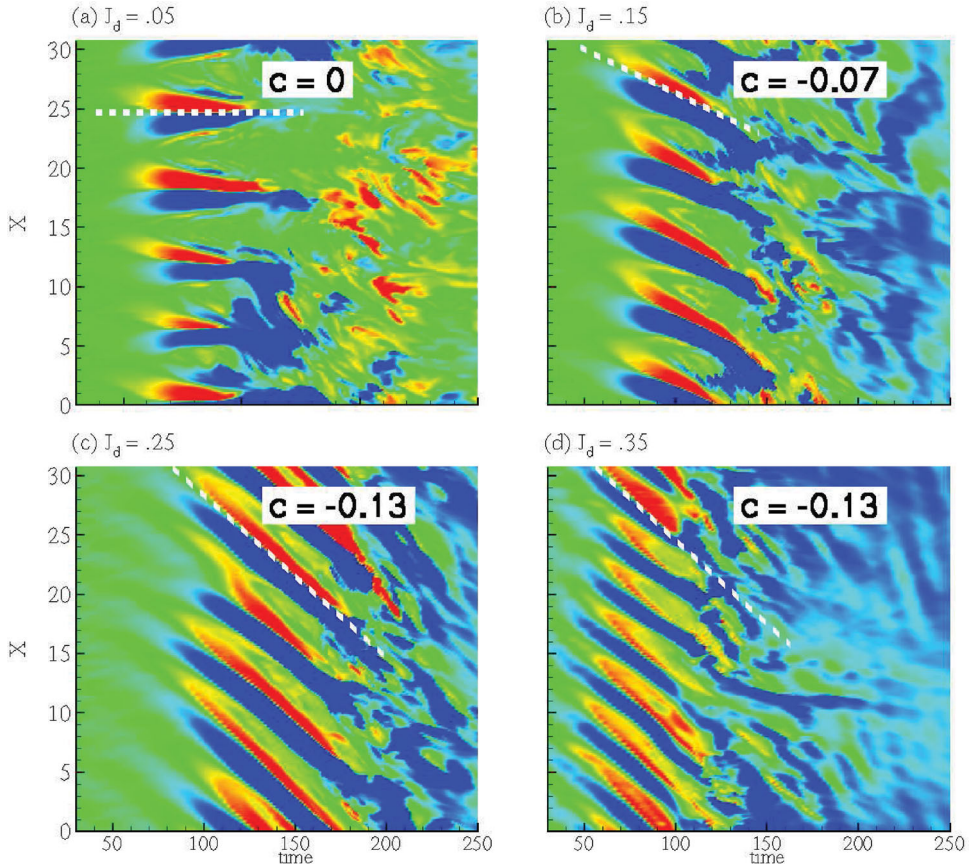


Figure 3. Phase speed of the shear instabilities is shown in $x-t$ diagrams of a density probe taken at $y = 3.6$ and $z = 0$. In the symmetric case of $J_d = 0.5$ (a), the phase line is horizontal denoting a zero phase speed of a *stationary* unstable mode. In other cases (b–d), the phase lines tilt downward, indicative of *propagating* unstable modes. Dotted lines denote phase lines whose slope is equal to the phase speed. Colour scale ranges from 0.997 (red) to 1.003 (blue).

of $J_d = 0.15$ and 0.25 . Density overturns are seen at $x = 2$ in Figure 4(b) and at $x = 14$ and 20 in Figure 4(c). Secondary density overturns have been reported in previous studies [4,9,12]. The DNS of H shear instability in Pham et al. [4] illustrates the development of secondary KH-like overturns on the cusps of the primary H waves. The secondary KH-like overturns in that study penetrates downward and causes intermittent patches of turbulent mixing in the lower half of the shear layer. In the present study, the secondary overturns also penetrate downward and cause mixing, as shown in Figure 4(b) and 4(c).

4. Internal wave field

Shear instability in flows with stratification that extends beyond the shear layer can excite internal waves that transport momentum and energy to regions far away from the shear layer. The conditions for the waves to be excited as well as the characteristics of the wave fields have been shown in previous studies to follow linear wave theory. The wavelength, frequency and propagating angles of the internal waves match with those of the KH shear instability

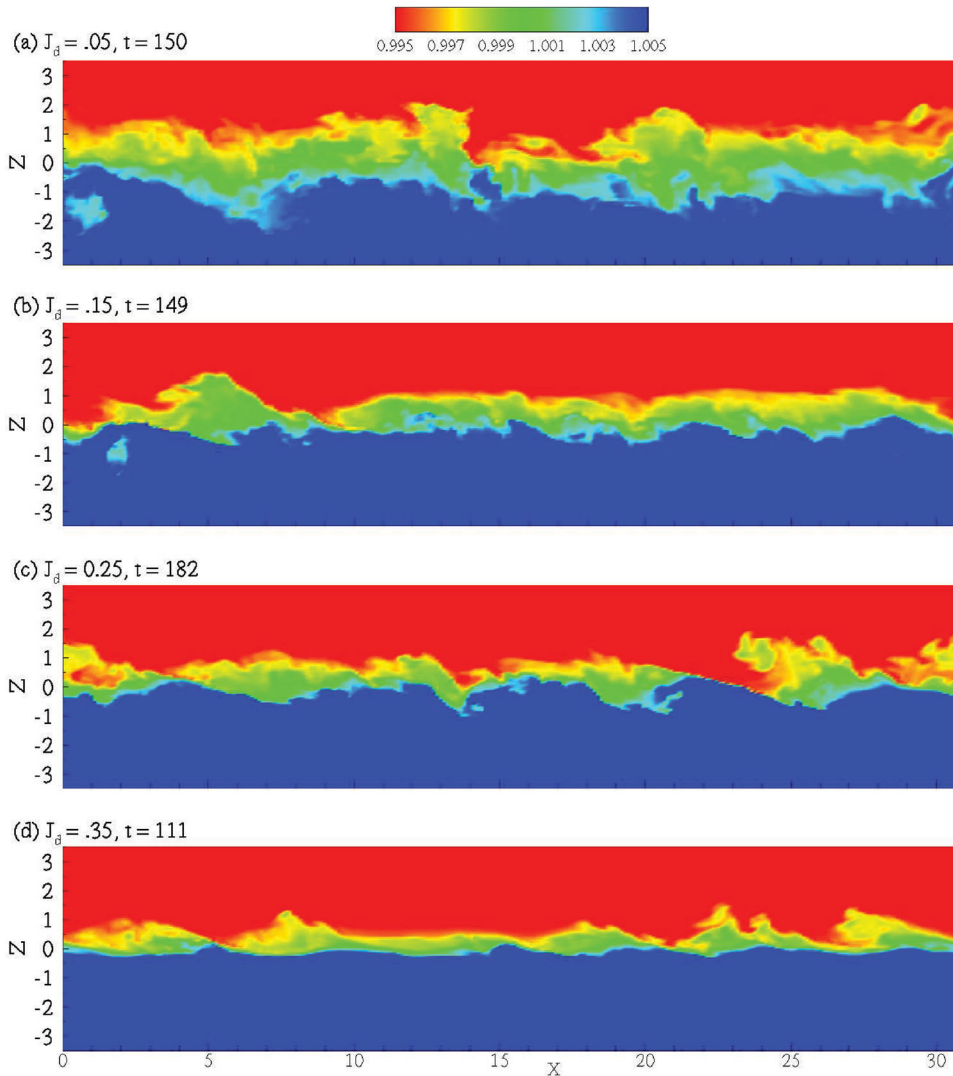


Figure 4. Snapshots of the density fields show transition into turbulence in the shear layer. The snapshots are shown at times when the integrated dissipation rate peaks. As J_d increases (a–d), the turbulent layer becomes thinner and concentrates toward the upper half of the shear layer where the stratification is weaker.

in the previous studies, e.g. [19]. The shear instabilities in the present study cannot directly excite internal waves; however, internal waves having different wavelengths are observed in regions below the shear layer. In this section, we will provide an explanation why the shear instabilities cannot excite waves and discuss the properties of the waves observed at depths.

Linear wave theory suggests that an internal wave can propagate in a stratified medium when its squared vertical wavenumber m^2 is positive in the medium. The squared vertical wavenumber m^2 is derived from the Taylor–Goldstein equation and takes the following

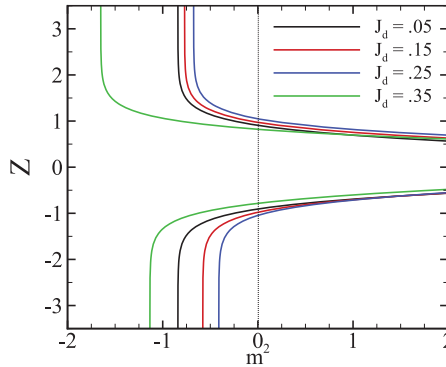


Figure 5. Squared vertical wavenumber m^2 shows negative values in regions below the shear layer in all simulated cases, and therefore, the shear instabilities cannot excite internal waves into this region.

form:

$$m^2 = \frac{N^2}{[c - \langle u \rangle]^2} + \frac{\partial^2 \langle u \rangle / \partial^2 z}{c - \langle u \rangle} - k^2, \quad (9)$$

where c is the wave phase speed and k is the horizontal wavenumber. From Figure 3, the horizontal wavenumber k of the shear instabilities is found to be 1.42 in the case of $J_d = 0.35$, and 1.02 in the other three cases. With the phase speeds given in Figure 3 and the initial mean profiles of velocity and stratification, the profiles of m^2 are plotted in Figure 5. In all cases, values of m^2 are negative in the region below the shear layer, and therefore, the shear instabilities cannot excite internal waves into this region. The DNS of Pham et al. [19] shows wave excitation by KH shear instabilities in the cases with $J_d > 0.18$. In the present study, wave excitation does not occur in the cases with $J_d = 0.25$ and 0.35 because the characteristics of the shear instabilities in the present study are different. In both these cases, the wavelength is shorter and the phase speed has a negative value. From Equation (9), a shorter wavelength would have a larger wavenumber k making m^2 become smaller. A negative phase speed c would cause the denominator in the first term on the right-hand side of Equation (9) to be larger since $\langle u \rangle$ is positive in the region below the shear layer. With a larger denominator, the first term would become smaller. Furthermore, a negative phase speed also makes the second term on the right-hand side of Equation (9) to become more negative. As a net result, a negative phase speed tends to make m^2 become smaller and negative in the region below the shear layer and prevents wave excitation into the region.

Nevertheless, internal waves are seen in the region below the shear layer. Wave momentum flux $\langle u'w' \rangle$ in Figure 6(a) and wave energy flux $\langle p'w' \rangle$ in Figure 6(b) measured at depth $z = -5$ indicate multiple bursts of internal waves propagating down from the shear layer in all four cases. In the case of $J_d = 0.05$, there are discrete peaks in the wave fluxes at times $t = 114, 170$ and 208 , and a later peak has a higher amplitude than the previous one. While the primary shear instability in this case, as shown in Figure 2(a), cannot excite internal waves, the nonlinear evolution of the shear instabilities can generate density perturbations

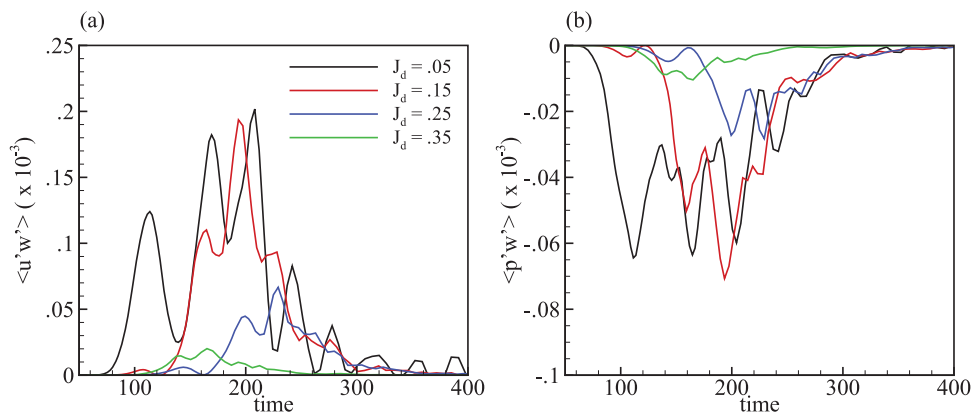


Figure 6. Vertical fluxes at depth $z = -5$ indicate multiple bursts of internal waves propagating downward away from the shear layer in all four cases: (a) momentum flux $\langle u'w' \rangle$ and (b) energy flux $\langle p'w' \rangle$.

that can excite internal waves. It is noted that while the primary modes of the shear instabilities have negative m^2 , their subharmonics can have positive m^2 since the wavenumber k of the subharmonics is smaller. The subharmonics of the shear instabilities can excite waves into regions below the shear layer. Broadband turbulence can also excite internal waves [25]; however, visualisations of fluctuating density fields show wave bursts with discrete wavelength and constant propagation angle unlike those generated by broadband turbulence, as will be discussed below.

Multiple bursts of internal waves are seen in each of the simulated cases, and the wave characteristics differ from burst to burst. For illustration, Figure 7 shows the wave fields of the first burst in each case. The waves in the figures clearly have a wavelength different from the wavelength of the fundamental shear instability mode. Furthermore, the wavelength and wave angle are different among the cases. The wavelength and wave angles are difficult to identify in the cases of $J_d = 0.15$ and 0.35 . The case of $J_d = 0.05$ has wave propagation with the largest wavelength corresponding to a horizontal wavenumber $k = 0.2$. The wavelength in the case of $J_d = 0.25$ is shorter with a wavenumber $k = 0.4$. In the case of $J_d = 0.05$, the waves have a propagating angle $\theta = 39.8^\circ$ to the vertical, and is equal to 49.2° in the case of $J_d = 0.25$. Using a dispersion relationship for linear internal waves, $\Omega = N \cos \theta$, the frequency Ω is equal to 0.17 and 0.33 in the cases with $J_d = 0.05$ and 0.25 , respectively. These frequencies are significantly smaller than the buoyancy frequency in regions below the shear layer. Since these waves have a measurable discrete frequency, they are not excited by broadband turbulence in the shear layer. It is likely that the waves are excited by the subharmonics of the shear instabilities.

5. Evolution of the mean flow

In Section 3, we have shown with instantaneous snapshots of the density field that the shear layers evolve asymmetrically as J_d increases. The asymmetry in the stratification profiles between the upper and lower halves of the shear layer also affects the momentum fields. In the asymmetric cases, the stronger stratification in the lower half of the shear layer

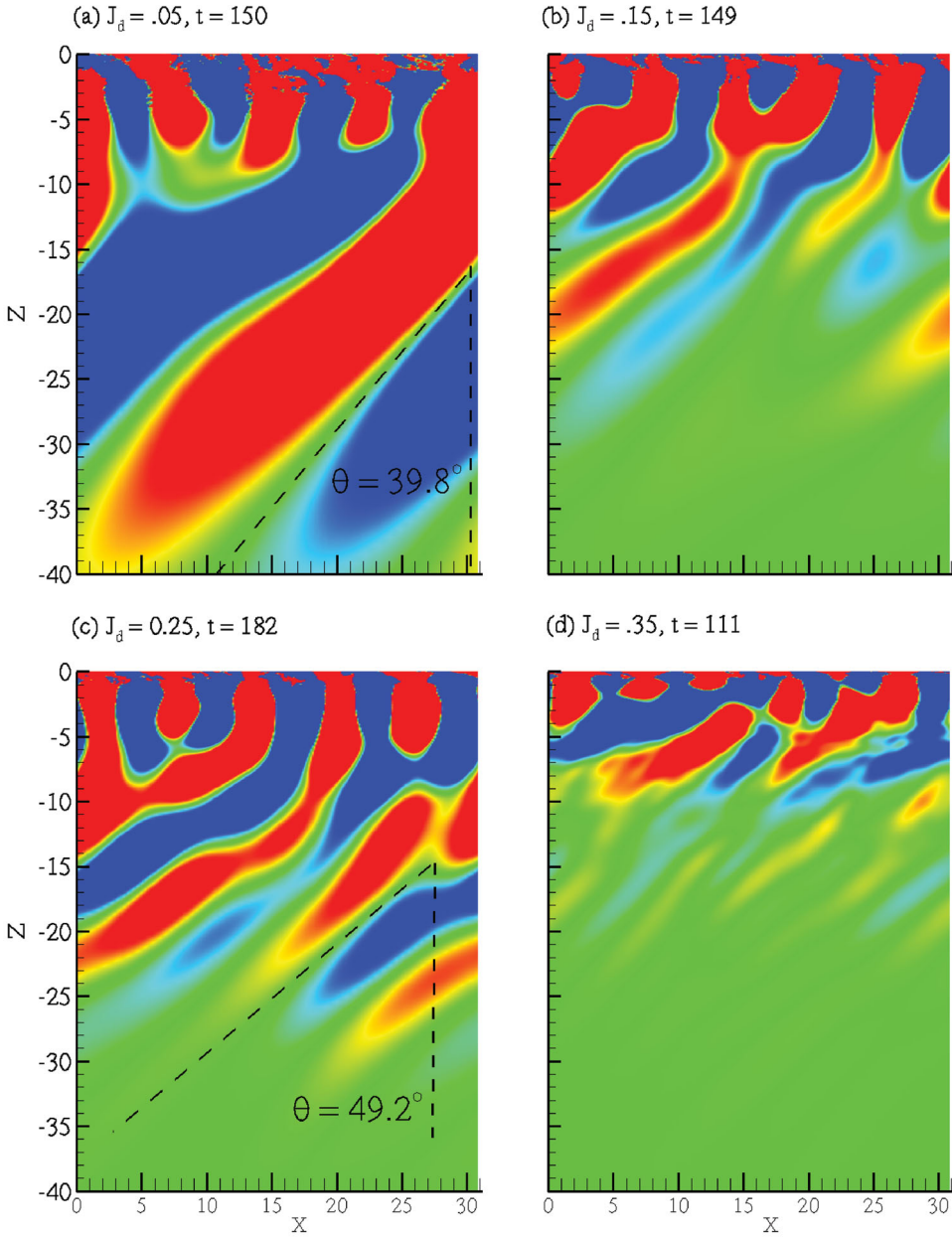


Figure 7. Snapshots of the fluctuating density fields ρ' show the structure of the internal wave fields. In all cases, the wavelength of internal waves at depths is different from that of the shear instabilities seen inside the shear layer.

reduces the ability of the shear instabilities and broadband turbulence to tap the momentum and kinetic energy available in the region. As a result, the thickness of the shear layer is reduced, the extraction of mean kinetic energy (MKE) into fluctuation energy is less, and the changes in mean profiles are skewed toward the upper half of the shear layer. In this

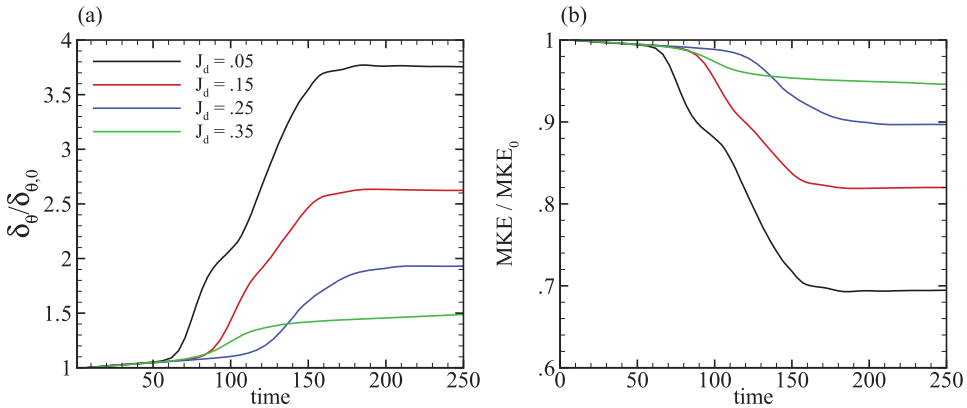


Figure 8. (a) Evolution of momentum thickness δ_θ indicates a significant reduction in the growth rate of the shear layers as J_d increases. (b) Change in integrated MKE is also less as J_d increases.

section, we contrast these effects among the cases to illustrate the influences of asymmetry in the stratification.

Figure 8(a) depicts the evolution of the momentum thickness δ_θ which is defined as

$$\delta_\theta(t) = \int_{z_l}^{z_u} \left[\frac{1}{4} - \langle u(t) \rangle^2 \right] dz,$$

where z_l and z_u are the lower and upper bounds, respectively, of the computational domain excluding the sponge. In all cases, the evolution of δ_θ includes three distinct periods. During the first period, $t < 50$, the shear instability grows from infinitesimal perturbations leading to a gentle growth of δ_θ . During the second period, $50 < t < 150$, δ_θ exhibits a rapid linear growth. The thickness grows significantly due to the enlargement of the billows and the wisps shown in Figure 2 as well as by turbulent entrainment. Finally, during the third period, δ_θ plateaus at a constant value for the rest of the simulation, indicating that no more momentum is extracted from the background shear. In all cases, the final values of δ_θ are dictated by the growth rate and the duration of the second period. In the symmetric case of $J_d = 0.05$, this period begins early and has the longest duration. As a result, the final value of δ_θ is largest among the cases. This final value is also comparable to the values reported in previous studies of symmetric shear layer [9,10,24]. As J_d increases, like in the cases with $J_d = 0.15$ and 0.25 , the secondary period commences later and has a shorter duration. In these two cases, the stronger stratification in the lower half of the shear layer prevents the KH billows to enlarge as much as in the case of $J_d = 0.05$. The final value of δ_θ in the case of $J_d = 0.15$ is 30% smaller than that in the case of $J_d = 0.05$. In the case of $J_d = 0.25$, δ_θ is further reduced to about 50%. Increasing J_d significantly reduces the size of the KH billows and δ_θ grows less. In the case of $J_d = 0.35$ where H wisps are seen, even though the second period commences earlier than in the case of $J_d = 0.25$, it only lasts for a short time period. The momentum thickness grows the least in this case.

Similar to the reduction in the momentum thickness, the extraction of MKE is also less as J_d increases. Here, MKE is computed as $1/2\rho_0 \langle u \rangle^2$ and integrated from z_l to z_u . Figure 8(b) contrasts the evolution of the integrated MKE, and the case of $J_d = 0.05$ shows the largest extraction of MKE among the simulated cases. In this case, approximately 30% of the MKE is extracted by the shear instability and turbulence. In the cases of $J_d = 0.15$

and 0.25, the extraction is reduced to 18% and 10%, respectively. The extraction is only 5% in the case of $J_d = 0.35$. A reduction in the extraction of MKE is a precursor for a reduction in turbulent production, and therefore, terms in TKE budget are significantly altered, as will be discussed in the next section.

The evolution of mean shear and stratification differs qualitatively among the cases with changes from the initial shape being increasingly skewed with increasing J_d owing to the asymmetric influence of buoyancy. Figure 9(a) and 9(b) contrasts the mean shear profiles $d\langle u \rangle/dz$ between the symmetric case of $J_d = 0.05$ and the asymmetric case of $J_d = 0.25$, respectively. In the case of $J_d = 0.05$, the shear profiles shown at three different times remain symmetric across the centre of the shear layer, $z = 0$, throughout the evolution of the shear instability. During the growth of the KH billows between times $t = 0$ and 78, the shear at $z = 0$ is reduced and the profiles thicken. When the shear layer becomes turbulent, the shear profile at $t = 150$ has peaks at the upper and lower edges of the shear layer. The peaks are symmetrically displaced from the centre of the shear layer. The peak in shear at the lower edge at this time coincides with the density overturns in the same region, as shown in Figure 4(a). Different from the case of $J_d = 0.05$, the shear profiles in the case of $J_d = 0.25$ shown in Figure 9(b) exhibit asymmetry across $z = 0$. Between times $t = 0$ and 136 when the KH billows develop, the shear at the centre is reduced, and the profiles thicken similar to the case of $J_d = 0.05$. However, the thickening is uneven with the upper half of the shear layer growing more. At time $t = 136$, the shear magnitude in the upper half is significantly smaller than that in the lower half. At time $t = 182$, the turbulence in the upper half of the shear layer continues to extract more energy and drives the shear further down. Meanwhile, the shear magnitude in the lower half increases. The asymmetric evolution in the shear profiles is consistent with the reduction in MKE extraction. Due to the strong stratification in the lower half of the shear layer in the case of $J_d = 0.25$, the shear instability cannot extract MKE in this region. The extraction of MKE is substantial only in the upper half, leading to a significant reduction of the mean shear.

Similar to the evolution of the shear profiles, the profiles of N^2 at various times are symmetric in the case of $J_d = 0.05$, as shown in Figure 9(c). The N^2 profiles in this case have values in the centre of the shear layer that decrease in time due to mixing. Stratification at the edges of the shear layer gets stronger in time with values larger than the initial stratification. Overshoot in N^2 profiles at the edges of the shear layer has been noted in previous studies [19,24] too. The overshoot in the case of $J_d = 0.05$ is symmetric across $z = 0$ at both times $t = 78$ and 150. In the case of $J_d = 0.25$, the N^2 profile, which is initially asymmetric, also exhibits overshoots at later times as the shear layer evolves, as shown in Figure 9(d). However, the overshoots occur closer to the centre of the shear layer when compared with the case of $J_d = 0.05$. When the N^2 profile at late time is compared to the initial profile, the case of $J_d = 0.05$ shows a significant reduction in N^2 over the entire shear layer $-1 < z < 1$. The mixing is equally efficient between the upper and lower halves of the shear layer. In contrast, the reduction of N^2 in the case of $J_d = 0.25$ is only notable in a thin region immediately below the centre of the shear layer, $-0.25 < z < 0$. While the instability level in the case of $J_d = 0.25$ occurs in the upper half of the shear layer and a large amount of MKE is extracted in this region, mixing is most significant in the lower half where the stratification is initially large.

The evolution of the gradient Richardson number Ri_g is depicted in Figure 9(e) and 9(f) for the cases of $J_d = 0.05$ and 0.25, respectively. In both cases, Ri_g grows to larger values at the centre of the shear layer, and the values are greater than 1 at the end of the simulations. Furthermore, both cases show profiles of Ri_g having local *minima* at the *edges* of the shear

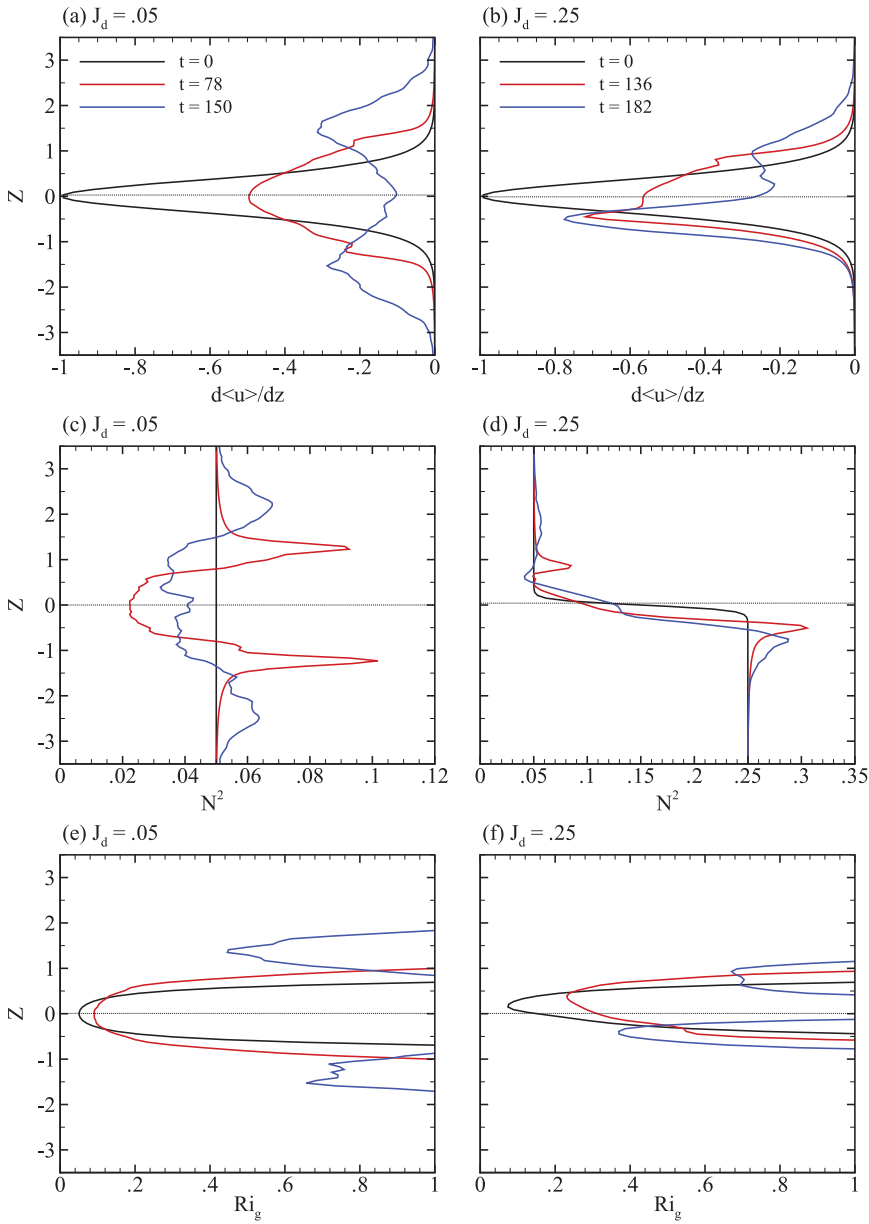


Figure 9. Differences in the mean profiles between symmetric $J_d = 0.05$ (a, c, e) and asymmetric $J_d = 0.25$ (b, d, f) shear layers. Evolution of mean shear $d\langle u \rangle / dz$ is shown in (a, b), squared buoyancy frequency N^2 in (c, d) and gradient Richardson number in (e, f). Colours indicate different times during the simulations.

layers at late time. The Ri_g minima are caused by the enhanced shear that develops in these regions. In the case of $J_d = 0.05$, the minimum Ri_g at the lower edge is larger than the value seen in the upper edge at time $t = 150$. This is due to the slight difference in the magnitude of $d\langle u \rangle / dz$ and N^2 between the edges, as shown in Figure 9(a) and 9(c). In the case of J_d

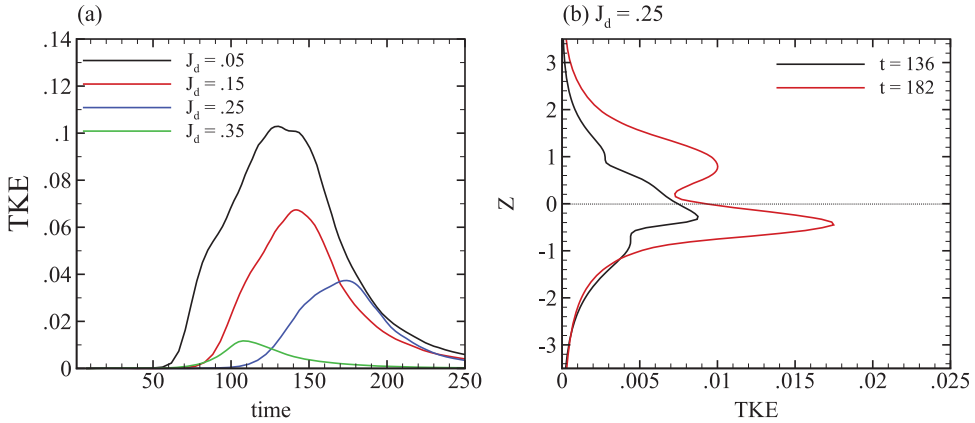


Figure 10. (a) TKE integrated across the shear layer $-5 < z < 5$ is smaller in the case of larger J_d . (b) Profiles of TKE at different times show asymmetry within the shear layer in the case of $J_d = 0.25$.

$= 0.25$, the shear and the stratification at the lower edge are significantly larger than the values at the upper edge, and Ri_g is smaller at the lower edge.

It is necessary to address the significance of small Ri_g in the lower half of the shear layer at late time in the case of $J_d = 0.25$. The value of $Ri_g \approx 0.35$ in this region is *marginally stable*, i.e. it is not significantly larger than the critical value for shear instability, $Ri_g = 0.25$. Furthermore, there is a large shear and strong MKE in this region. As KH billows develop in the upper half of the shear layer, the shear increases in the lower half and Ri_g decreases to marginal values in the lower half. The peak shear in the lower half at time $t = 182$ is 80% of the shear at $z = 0$ at initial time, as shown in Figure 9(b). The stability condition seen in the lower half of the shear layer in the case of $J_d = 0.25$ of the present study is similar to the observations in the upper flank of the EUC where marginally-stable Ri_g and strong shear are reported. The observations of Smyth et al. [26] and the numerical simulation of Pham et al. [27] indicate that a downward momentum flux from the region above the EUC can enhance the shear, cause Ri_g to be subcritical, and drive mixing in the marginally-stable EUC region. In the present study, the shear in the lower half of the shear layer does not increase enough to drive Ri_g below 0.25.

6. Turbulent kinetic energy

In the previous section, we have shown that the extraction of MKE decreases as the stratification J_d increases. In the present study, the initial MKE is the only source of energy that can be used to generate turbulence and mix the fluids. With a lower amount of MKE extraction, the TKE is significantly reduced. In this section, we analyse the TKE budget to illustrate how the stratification in the lower half of the shear layer affects the terms in the budget. Specifically, all terms in the budget are shown to decrease as J_d increases. The profiles of the terms in the TKE budget are asymmetric across the centre of the shear layer, similar to the discussed mean profiles.

The amount of TKE extracted from the reservoir of background shear is shown in Figure 10(a) for the four simulated cases. The values plotted in the figure are integrated over the shear layer in the region $-5 < z < 5$. In the figure, the peak values of TKE decrease as J_d increases. The peak value in the case of $J_d = 0.35$ is only 10% of the value in the case

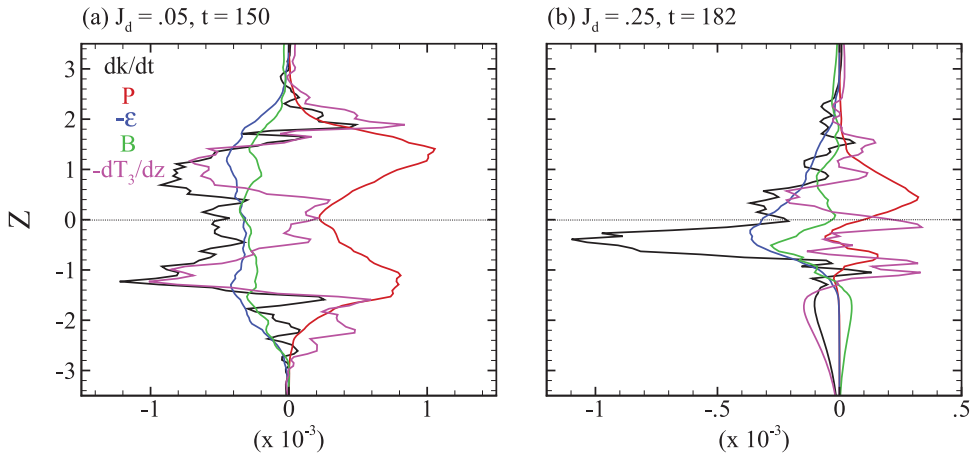


Figure 11. TKE budgets in the shear layer exhibit symmetry in the case of $J_d = 0.05$ (a) and asymmetry in the case of $J_d = 0.25$ (b). Colours indicate different terms in the budget.

of $J_d = 0.05$. In the three cases with KH billows, $J_d = 0.05, 0.15$ and 0.025 , the peak TKE occurs earlier and has a larger magnitude in the case of smaller J_d . However, the integrated TKE is comparable at late time $t = 250$ in the three cases. It is noted that the peak TKE occurs earlier than the time when the MKE begins to plateau in Figure 8(b). In the case of $J_d = 0.05$, the TKE peaks at time $t = 128$ while the MKE does not plateau until $t > 150$. As KH billows break down to turbulence, the MKE is continued to be extracted; however, the TKE does not increase any longer. The dissipation rate becomes significant during this time, causing the integrated TKE to deplete.

As J_d increases, the profiles of TKE exhibit asymmetry as the shear layer evolves. Figure 10(b) shows TKE profiles at times $t = 136$ and 182 in the case of $J_d = 0.25$. Even though TKE increases in both the upper and the lower halves of the shear layer between the two times, the profiles are thinner in the lower half. The peak TKE occurs in the lower half of the shear layer at both times. It is noted that TKE in the present study includes both wave kinetic energy and broadband TKE. As the KH billows in the case of $J_d = 0.25$ develop in the upper half of the shear layer, it transports wave energy to the lower half. Since Figure 5 shows $m^2 > 0$ in the lower half of the shear layer, internal waves excited by the KH billows can propagate down into this region. The waves are trapped in this region since $m^2 < 0$ in the region below the shear layer. As the waves pile up in the lower half, this region has larger TKE than the upper half as seen at time $t = 136$ in Figure 10(b). Between times $t = 136$ and $t = 182$, TKE increases most significantly in the lower half of the shear layer and secondary density overturns occur as previously shown in Figure 4(c). The trapping of wave energy in the lower half of the shear layer as well as the secondary overturns has been noted in the DNS of an asymmetric H shear instability by Pham et al. [4].

The asymmetry is also observed in the profiles of the terms in the TKE budgets in the cases with large J_d . The budgets at times when the peak integrated dissipation occurs in the cases of $J_d = 0.05$ and 0.25 are contrasted in Figure 11(a) and 11(b), respectively. In the symmetric case of $J_d = 0.05$, the production has peaks at the edges of the shear layer where the magnitude of shear is maximum, as shown in Figure 9(c). The peaks are equally displaced from the centre of the shear layer and have comparable values. The profiles of the dissipation and the buoyancy flux spread comparably in the upper and lower halves. In

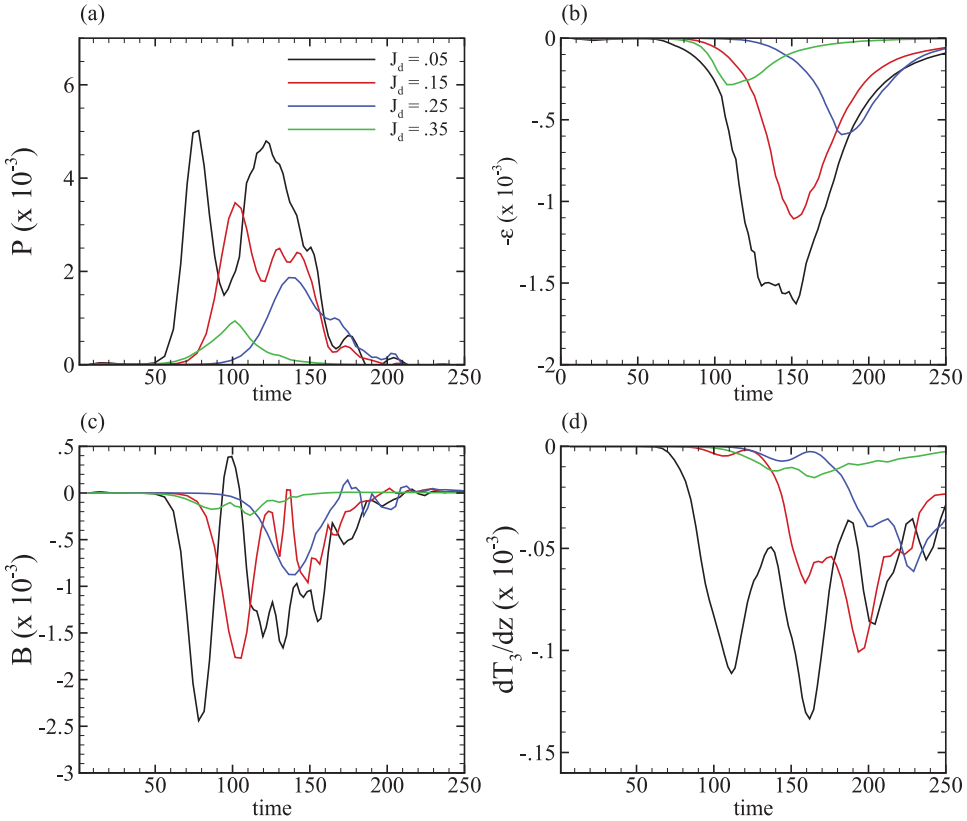


Figure 12. Integrated TKE budgets across the shear layer $-5 < z < 5$ show a reduction in all components: (a) production P , (b) dissipation ε , (c) buoyancy flux B and (d) transport dT_3/dz . Colours indicate different cases.

the asymmetric case of $J_d = 0.25$, the production profile is asymmetric with a large peak in the upper half and a smaller peak in the lower half. The profile of the buoyancy flux indicates an opposite trend with a larger peak in the lower half. It is interesting that when the integrated dissipation is maximum, most of the dissipation occurs in the lower half of the shear layer where the stratification is large. The large dissipation and buoyancy flux in the lower half of the shear layer are the results of secondary density overturns which have been discussed in previous sections.

As the stratification J_d increases, the production, dissipation, buoyancy flux and transport integrated over the shear layer $-5 < z < 5$ are all reduced as shown in Figure 12. The peak value in the integrated production in Figure 12(a) is largest in the case of $J_d = 0.05$ and progressively decreases with increasing J_d . The peak production in the case of $J_d = 0.35$ is only 20% as large as the peak in the case of $J_d = 0.05$. When Figure 12(a) is compared to Figure 10(a), the integrated production peaks at the same time as the integrated TKE in the case of $J_d = 0.35$. In the other three cases, the production peaks significantly earlier than the TKE. In the case of $J_d = 0.05$, the production peaks at time $t = 78$ but the TKE does not peak until $t = 130$ when a second peak in production occurs. Similarly, in the case of $J_d = 0.25$, the production peaks at time $t = 136$ and the TKE peaks later at $t = 178$. In the cases with KH billows, $J_d = 0.05, 0.15$ and 0.25 , TKE continues to increase for an

extended period after the KH billows break down. However, as the H wisps in the case of $J_d = 0.035$ break down, the TKE immediately decreases. The lag between large coherent structures and small-scale turbulence is short-lived during the evolution of H instability.

While the peak production occurs early in the case of $J_d = 0.05$, the dissipation rate in Figure 12(b) peaks early in the case of $J_d = 0.35$. The peak dissipation rate occurs immediately after the peak production in this case. Among the cases, the case of $J_d = 0.05$ has the largest peak in the dissipation. Similar to the production, the peak values decrease as J_d increases. The peak dissipation in the case of $J_d = 0.35$ is only 18% of the peak value seen in the case of $J_d = 0.05$. A similar trend is found in the integrated buoyancy flux and the integrated transport, shown in Figure 12(c) and 12(d), respectively. In the study of Pham et al. [19], the total wave energy transport over the entire evolution of the shear layer can be as large as 33% of the integrated dissipation. The wave energy flux in the present study is significantly weaker. As shown in Figure 6(b), the wave energy flux $\langle p'w' \rangle$ across the depth $z = -5$ integrated over the simulation is only 17% of the integrated dissipation in the case of $J_d = 0.05$.

7. Conclusions

We have performed LESs to investigate the evolution of an asymmetric turbulent shear layer. Unlike previous studies, the density in the present study is continuously stratified throughout and beyond the shear layer. Furthermore, the stratification profiles used here are asymmetric with the upper and lower halves of the shear layer having different values for the density gradient. We fix the stratification in the upper half and vary J_d in four cases.

We extend the previous DNS and LSA of Carpenter et al. [14,15] on the evolution of asymmetric H shear instabilities. We find that varying the stratification in the lower half of the shear layer over a small range of values leads to qualitative differences in the initial shear instability as well as the ensuing turbulence. This sensitivity to the level of stratification is the main conclusion of the present work.

Shear instability progressively changes from a pure KH mode, passing through a mixed mode, to a pure H mode with increasing J_d . Although the present background profiles are different from the eccentric shear/stratification profiles of Carpenter et al. [15], both studies have initial asymmetry in the profile of gradient Richardson number, $Ri_g(z)$. It is the increasing asymmetry in $Ri_g(z)$ that leads to a similar progression of instabilities in the present work and that of Carpenter et al. [15]. In the symmetric case where the stratification is the same throughout the shear layer, $J_d = 0.05$, a stationary KH shear instability develops at the centre of the shear layer and the central isopycnal rolls up. In the asymmetric case with largest stratification, $J_d = 0.35$, an H shear instability grows with the instability level in the upper half of the shear layer. The H instability has a negative phase speed and a wavelength shorter than that of the KH shear instability. In the asymmetric cases of $J_d = 0.15$ and 0.25 , a propagating shear instability is observed in the upper half of the shear layer. The shear instability has mixed characteristics: negative phase speed as in the H regime and overturned isopycnals similar to the KH mode in the upper half of the shear layer. As J_d increases, the phase speed also increases and the instability level, where the instability initially grows, is displaced further above the centre of the shear layer. The nonlinear evolution of the KH instability involves the formation of KH billows, secondary density overturns and turbulence, while the evolution of the H instability shows the formation of density wisps and turbulence. Neither the fundamental KH nor H shear instability excites internal waves in the present study, although bursts of internal waves having a longer

wavelength associated with nonlinear evolution of other discrete instability modes are seen in regions below the shear layer.

Due to asymmetry in the initial density profile, the evolution of the mean profiles and turbulent kinetic budgets is also asymmetric. As J_d increases, the growth of the momentum thickness is significantly reduced as well as the extraction of the MKE. Fluctuations draw energy from the background shear reservoir, mostly in the upper half of the shear layer with weaker stratification. Surprisingly, during the period when the integrated turbulent dissipation is large, the case of $J_d = 0.25$ shows the largest turbulent dissipation in the *lower*, strongly stratified half of the shear layer. The reason is that the asymmetric stirring, stronger in the upper half of the sheared region, is responsible for the lower half having a relatively larger shear and a relatively smaller value of Ri_g that is marginally stable with a value of 0.35. Secondary density overturns in this region lead to enhanced small-scale turbulence and dissipation.

The present study extends the previous DNS study of Carpenter et al. [14] on asymmetric H shear instability. Similar to their results, we found that the evolution of the shear instabilities and the resulting turbulence depends strongly on the degree of asymmetry in the shear layer. Carpenter et al. [14] create the asymmetry by displacing the density interface between two layers of constant density away from the centre of the shear layer. In contrast, the asymmetry in the present study is due to differences in the density gradient between the top and bottom halves of the shear layer. This type of asymmetry has direct applications into many geophysical flows such as the EUC. In the EUC, the stratification in the sheared region near the surface mixed layer is typically weaker than the stratification in the sheared undercurrent. Results from the present study suggest that there is a wide range of shear instabilities, i.e. asymmetric H shear instability, that can develop in the EUC besides the traditional KH shear instability.

Funding

We gratefully acknowledge the support provided by the National Science Foundation [grant number OCE-1355856, programme monitor E. Itsweire].

References

- [1] W.R. Geyer, A.C. Lavery, M.E. Scully, and J.H. Trowbridge, *Mixing by shear instability at higher Reynolds number*, Geophys. Res. Lett. 37 (2010), pp. 1–5.
- [2] T. Johnston and D. Rudnick, *Observations of the transition layer*, J. Phys. Oceanogr. 39 (2009), pp. 780–797.
- [3] J.N. Moum, J.D. Nash, and W.D. Smyth, *Narrowband oscillations in the upper equatorial ocean. Part I: Interpretation as shear instabilities*, J. Phys. Oceanogr. 41 (2011), pp. 397–410.
- [4] H.T. Pham, S. Sarkar, and K.B. Winters, *Near-N oscillations and deep-cycle turbulence in an upper Equatorial Undercurrent model*, J. Phys. Oceanogr. 42 (2012), pp. 2169–2184.
- [5] P. Hazel, *Numerical studies of the stability of inviscid stratified shear flows*, J. Fluid Mech. 51 (1972), pp. 39–61.
- [6] S.A. Thorpe, *Experiments on instability and turbulence in a stratified shear flow*, J. Fluid Mech. 61 (1973), pp. 731–751.
- [7] C.G. Koop and F.K. Browand, *Instability and turbulence in a stratified fluid with shear*, J. Fluid Mech. 93 (1979), pp. 135–159.
- [8] A. Alexakis, *Stratified shear flow instabilities at large Richardson numbers*, Phys. Fluids 21 (2009), p. 054108.
- [9] W.D. Smyth and J.N. Moum, *Length scales of turbulence in stably stratified mixing layers*, Phys. Fluids 12 (2000), pp. 1327–1342.

- [10] C.P. Caulfield and W.R. Peltier, *The anatomy of the mixing transition in homogeneous and stratified free shear layers*, J. Fluid Mech. 413 (2000), pp. 1–47.
- [11] E.J. Strang and H.J.S. Fernando, *Entrainment and mixing in stratified shear flows*, J. Fluid Mech. 428 (2001), pp. 349–386.
- [12] W.D. Smyth and K.B. Winters, *Turbulence and mixing in Holmboe waves*, J. Phys. Oceanogr. 33 (2003), pp. 694–711.
- [13] K. Brucker and S. Sarkar, *Evolution of an initially turbulent stratified shear layer*, Phys. Fluids 19 (2007), p. 101105.
- [14] J.R. Carpenter, G.A. Lawrence, and W.D. Smyth, *Evolution and mixing of asymmetric Holmboe instabilities*, J. Fluid Mech. 582 (2007), pp. 103–132.
- [15] J.R. Carpenter, N.J. Balmforth, and G.A. Lawrence, *Identifying unstable modes in stratified shear layers*, Phys. Fluids 22 (2010), pp. 1–13.
- [16] B. Sutherland and P. Linden, *Internal wave excitation from stratified flow over thin barrier*, J. Fluid Mech. 377 (1998), pp. 223–252.
- [17] B.R. Sutherland, *Rayleigh wave-internal wave coupling and internal wave generation above a model jet stream*, J. Atmos. Sci. 63 (2006), pp. 1042–1055.
- [18] K.L. Tse, A. Mahalov, B. Nicolaenko, and H.J.S. Fernando, *Quasi-equilibrium dynamics of shear-stratified turbulence in a model tropospheric jet*, J. Fluid Mech. 496 (2003), pp. 73–103.
- [19] H.T. Pham, S. Sarkar, and K.A. Brucker, *Dynamics of a stratified shear layer above a region of uniform stratification*, J. Fluid Mech. 630 (2009), pp. 191–223.
- [20] M. Germano, U. Piomelli, P. Moin, and W. Cabot, *A dynamic subgrid-scale eddy viscosity model*, Phys. Fluids 3 (1991), pp. 1760–1765.
- [21] S. Basak and S. Sarkar, *Dynamics of a stratified shear layer with horizontal shear*, J. Fluid Mech. 568 (2006), pp. 19–54.
- [22] K.A. Brucker and S. Sarkar, *A comparative study of self-propelled and towed wakes in a stratified fluid*, J. Fluid Mech. 652 (2010), pp. 373–404.
- [23] H.T. Pham and S. Sarkar, *Large-eddy simulations of a stratified shear layer*, J. Fluids Eng. 136 (2014), p. 061207.
- [24] H.T. Pham and S. Sarkar, *Transport and mixing of density in a continuously stratified shear layer*, J. Turbul. 11 (2010), pp. 1–23.
- [25] J.R. Taylor and S. Sarkar, *Internal gravity waves generated by a turbulent bottom Ekman layer*, J. Fluid Mech. 590 (2007), pp. 331–354.
- [26] W.D. Smyth, J.N. Moum, L. Li, and S.A. Thorpe, *Diurnal shear instability, the descent of the surface shear layer and the deep cycle of equatorial turbulence*, J. Phys. Oceanogr. 43 (2013), pp. 2432–2455.
- [27] H.T. Pham, S. Sarkar, and K.B. Winters, *Large-eddy simulation of deep-cycle turbulence in an Equatorial Undercurrent model*, J. Phys. Oceanogr. 43 (2013), pp. 2490–2502.